sustainability

MDPI

Article

Mechanism of Floor Failure During Coordinated and Sustainable Extraction of Coal and Geothermal Resources in Deep Mines: A Case Study

Jiakun Lv [1,2,3,*], Luchang Xiong [2,3,*], Jian Ma [1], Kun Yu [2,3], Wenxiao Cui [1], Zhen Zhang [1] and Zhuhua Yan [1]

[1] School of Naval Architecture & Ocean Engineering, Jiangsu University of Science and Technology, Zhangjiagang 215600, China
[2] School of Mines, China University of Mining and Technology, Xuzhou 221116, China
[3] Key Laboratory of Deep Coal Resource Mining (CUMT), Ministry of Education of China, School of Mines, China University of Mining & Technology, Xuzhou 221116, China
* Correspondence: 202400000007@just.edu.cn (J.L.); lchxiong@cumt.edu.cn (L.X.); Tel.: +86-156-2400-8533 (J.L.); +86-151-6211-0759 (L.X.)

Abstract

Achieving the sustainable development and utilization of mining energy resources necessitates the promotion of coordinated extraction of coal and geothermal resources. However, the direct discharge of untreated mine water not only leads to the dual wastage of water and geothermal resources but also poses environmental risks such as heavy metal contamination. Consequently, establishing an integrated green mining model that combines the recovery of coal, water, and geothermal energy has become an imperative for the sustainable development of the industry. Within this context, ensuring the stability of the floor strata during simultaneous coal mining and geothermal extraction represents a critical scientific challenge determining the safe and efficient implementation of this integrated technology. This study first presents the overall framework of a Simultaneous Extraction of Coal and Geothermal Resources (SECGR) technical system. Subsequently, through theoretical modeling and numerical simulation, we systematically studied the dynamic stress redistribution patterns and failure mechanisms within the bottom strata during the mining disturbance and extraction unloading process (MD-EU). The findings reveal that the vertical stress field exhibits an asymmetric distribution under the combined mining operations, while the shear stress field forms a distinctive saddle-shaped arch structure. The failure process of the floor strata undergoes four typical stages: the pristine state, crack initiation, crack propagation, and crack coalescence. Based on this, three characteristic zones are identified: the mining-induced failure zone, the water-resistant zone, and the unloading-activated zone. Finally, the Burgers viscoelastic model is employed to successfully quantify the time-dependent evolution of rock mass damage following mining-induced stress release. The research outcomes provide crucial theoretical support and technical guidance for safely advancing multi-energy coordinated extraction and enhancing the comprehensive resource utilization efficiency of mining systems.

Keywords: co-exploitation of coal and geothermal energy; floor failure depth; hydro-mechanical modeling; numerical simulation; unloading

check for updates

Academic Editor: Jin Luo

Received: 14 October 2025
Revised: 7 November 2025
Accepted: 13 November 2025
Published: 19 November 2025

Citation: Lv, J.; Xiong, L.; Ma, J.; Yu, K.; Cui, W.; Zhang, Z.; Yan, Z. Mechanism of Floor Failure During Coordinated and Sustainable Extraction of Coal and Geothermal Resources in Deep Mines: A Case Study. *Sustainability* **2025**, *17*, 10341. https://doi.org/10.3390/su172210341

Copyright: © 2025 by the authors. Licensee MDPI, Basel, Switzerland. This article is an open access article distributed under the terms and conditions of the Creative Commons Attribution (CC BY) license (https://creativecommons.org/licenses/by/4.0/).

1. Introduction

The world's energy system is subjected to substantial changes [1]. In this context, China has outlined a two-stage carbon reduction target, reinforcing its commitment to a

low-carbon transition [2]. Nonetheless, the continued dominance of coal in the energy mix underscores the structural challenges in achieving a sustainable energy pathway. There is thus an urgent need to accelerate the shift toward clean energy systems, particularly those leveraging geothermal resources [3]. A critical issue in hydrothermal mining regions is the discharge of large volumes of untreated mine water, which not only leads to the loss of valuable water and thermal energy but also introduces contaminants such as heavy metal ions into surface water systems, farmland, and drinking water sources. To align with sustainable development goals, it is essential to adopt integrated strategies that recover both water and heat from mine discharges, thereby reducing environmental harm and enhancing resource efficiency [4,5]. The utilization of mine water, heat, and associated karst aquifers represents a promising opportunity to turn waste into wealth. The Symbiotic Extraction of Coal and Geothermal Resources (SECGR) system offers a viable model for integrated resource management. By utilizing existing mine infrastructure and subsurface data—such as formation permeability, thermal conductivity, and geothermal gradients—the system supports accurate identification of geothermal target zones. Repurposing mine installations including ventilation shafts, drainage networks, and tunnel supports can reduce initial drilling investments by approximately 35–40%. Moreover, the circulation of low-temperature fluids during geothermal operation extracts heat from coal seams, simultaneously mitigating underground thermal pollution through efficient heat exchange. Therefore, addressing the key scientific challenges related to the safe and efficient implementation of SECGR technology is of strategic importance for advancing sustainable energy transition and fostering the synergistic management of coal, water, and geothermal resources [6] (Figure 1).

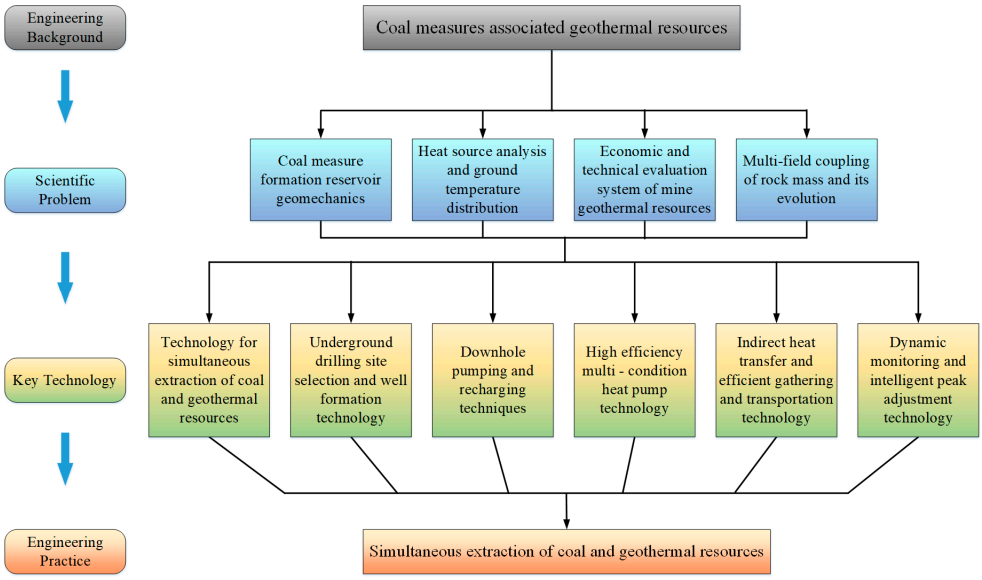


Figure 1. Framework of SECGR.

During the implementation of the SECGR technology system, one of the key problems is the stress evolution law and failure characteristics of coal seam floor under coupling of mining disturbance and karst heat storage negative-pressure extraction, namely extraction unloading (hereafter referred to as under MD-EU coupling). To date, scholars have conducted extensive studies on the stress evolution law and failure characteristics of coal seam floor by methods such as theoretical calculation [7,8], numerical simulation [9], similar materials [10,11] and in situ testing [12]. In terms of theoretical calculation, Slesarev [13] of the former Soviet Union theoretically analyzed the floor strata and established a theoretical formula for predicting water inrush from the floor. Wang et al. [14] deduced the

formula for calculating the maximum failure depth of coal seam floor according to the stress distribution there. Meng et al. [15], Zhu et al. [16], and Song and Liang [17] studied the stress distribution and failure characteristics of coal seam floor based on the abutment pressure distribution in front of the working face and the rock mass limit equilibrium theory. Many scholars put forward theories to analyze the failure characteristics of coal seam floor, including the water inrush coefficient [18], lower three zones theory [19], the in situ tensile theory and the zero failure theory [20]. As for numerical simulation, Tang [21] is the first to propose the heterogeneous rock fracture process analysis (RFPA) program, which provided a direct understanding of the initiation, propagation and penetration of coal seam floor cracks and the formation of water gushing channels around faults. Lu and Yao [22] and Wang et al. [14] made damage and flow modeling based on micromechanics coupling for mining in a confined aquifer, and successfully simulated the gradual development of fractures and the redistribution of stress. Moreover, various multi-field coupling methods including thermal–water–force–machinery coupling [23], fluid–solid coupling [24] and thermal–water–force–force–chemistry coupling [25] models have been proposed. In terms of laboratory experiment, Feng et al. [26] adopted the self-designed confined water loading system of coal seam floor to simulate the effect of confined water bag on floor waterproof layer, and determined the maximum development depth of floor cracks. Zhang et al. [27] researched the interaction between floor rock cracks and stress and seepage fields through physical simulation and obtained the evolution law of water inrush from floor cracks under fluid–solid coupling. With respect to in situ testing, Cheng et al. [28] used the wave velocity of rock mass to test the state of rock mass and determined the development range of water-conducting fractures in floor failure.

Various methodologies have been employed to assess floor failure characteristics. Su and Wei [29] utilized resistivity tomography technology to monitor floor damage. In investigations into predictive formulas, Gao et al. [30,31] accounted for multiple influencing factors and correspondingly applied a nonlinear regression analysis to fit the relationship between these factors and the measured floor failure depth. Furthermore, Wu et al. [32] developed water inrush prediction models specifically for the Donghuantuo and Zhangcun Coal Mines, providing a theoretical foundation for safety mining.

Although prior research has significantly advanced our understanding of stress evolution and failure characteristics in coal seam floors, most investigations have primarily focused on the influence of isolated factors. Consequently, these studies fail to adequately represent the complex mechanical behavior of the floor under the coupled effects of mining-induced disturbance and the pressure relief from a confined aquifer.

Moreover, in the new technical mode of SECGR, there is still a lack of knowledge and research on the stress evolution law and failure characteristics of coal seam floor under MD-EU coupling. And the corresponding theoretical model remains insufficient. Therefore, it is thus essential to develop a mechanical model under MD-EU coupling in order to accurately determine the stress evolution and failure characteristics of the coal seam floor during the SECGR process. These efforts are crucial for predicting and evaluating the feasibility of the SECGR technology system.

This study focuses on the mechanical behavior of coal seam floor under MD-EU coupling during SECGR. First, the geothermal geological background of Pingdingshan coalfield was analyzed to design the SECGR technology system. Next, considering the coupling effect of mining disturbance and extraction unloading, a hydraulic model was established to analyze the stress evolution law of coal seam floor and quantify the failure characteristics of floor under the coupling effect. Moreover, the FLAC3D fluid–solid coupling numerical model was established, and the failure characteristics of coal seam floor under MD-EU coupling were verified. Finally, the validity of the research was verified by

comparing theoretical and numerical simulation results. Furthermore, the influence of the unloading time on the failure characteristics of the floor was investigated.

The research results act as a basis for the field application of the SECGR technology system.

2. Engineering Background

2.1. Geothermal and Geological Background of Pingdingshan Coalfield

The co-occurrence of coal measures and geothermal resources in the Pingdingshan coalfield is attributed to its unique geological structure, wherein the Caledonian uplift in the eastern mining area led to surface denudation and the formation of a quasi-plain [33]. Multiple phases of tectonic activity induced lithospheric rupture and widespread development of deep faults, while more recent crustal extension and tectonic friction triggered mantle upwelling, collectively establishing a high geothermal background in the basin [34,35]. Recent heat flow compilations indicate values between 60 mW·m^{-2} and 80 mW·m^{-2} in the coalfield, exceeding both the Chinese (60.4 mW·m^{-2}) and global continental (64.7 mW·m^{-2}) averages [36]. These elevated heat flow and geothermal gradient conditions signify substantial subsurface thermal energy storage, highlighting significant geothermal potential. Mapping the heat flow distribution in the eastern mining area (Figure 2) facilitates the identification of favorable zones for geothermal exploitation. This tectonically mediated association of coal and geothermal resources not only confirms the area's suitability for geothermal development but also provides a natural basis for implementing the Synergistic Extraction of Coal and Geothermal Resources (SECGR) technology system.

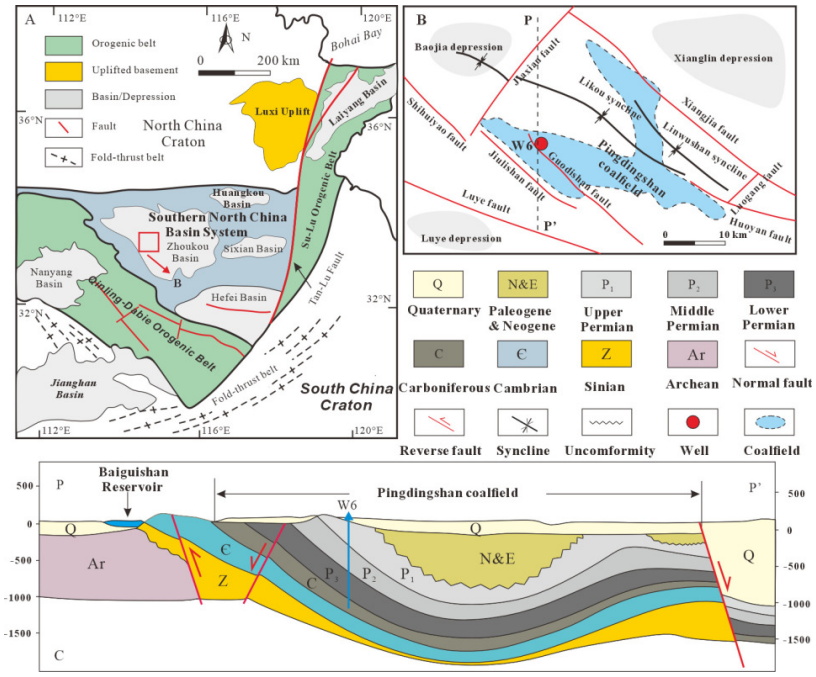


Figure 2. Geological maps of Pingdingshan coalfield. (**A**) Geological map and location of the basin system in southern North China. (**B**) structural outline map of Pingdingshan coalfield and its surroundings. (**C**) Stratigraphic map of Pingdingshan coalfield.

2.2. Design of the SECGR Technology System

The SECGR technology system was constructed in the hope of developing and utilizing the geothermal resources and realizing SECGR. The geothermal geology in Pingdingshan coalfield being the engineering background, the SECGR technology system integrates the mine production system and the geothermal well group layout technology and takes No. 10 Mine of Pingdingshan Tianan Coal Co., Ltd. (Pingdingshan, China). in the eastern coalfield as the technical implementation mine. The overall scheme is shown in Figure 3.

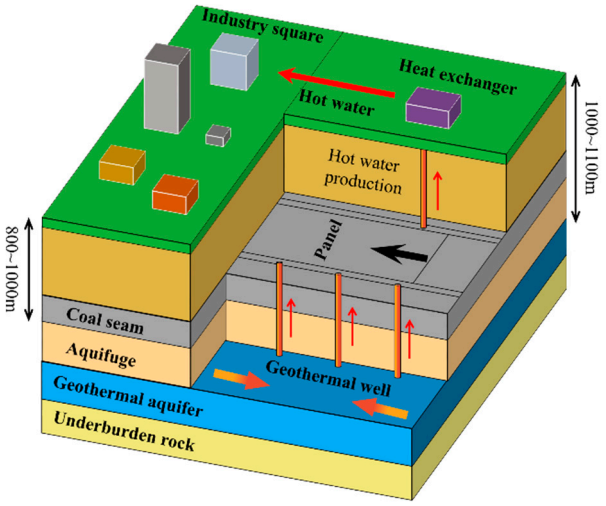


Figure 3. Sketch map of the SECGR technology system.

The SECGR technology system was developed as follows: First, a mine geothermal utilization system which mainly relied on the heat exchange station was built on the well to exchange low-quality heat energy such as drained mine water and deep hot water, and the geothermal water resources after heat exchange were supplied to the industrial square for production and life. Second, a SECGR system comprising a coal production system, a geothermal well group system and a water storage system was built underground. The SECGR system ensured that the mining of underground coal resources and the negative-pressure extraction of karst heat storage were conducted simultaneously, and it collected the heat energy of gushing mine water and deep geothermal water. In this way, the on-site application of the SECGR technology system was realized. The specific mining process is as follows: The extraction, drainage and pressure relief of karst heat reservoir were completed before mining to ensure the safety of mining activities. Based on the principle that coal seam extraction generates an altered stress field and an associated fracture network, the SECGR technology facilitates geothermal reservoir stimulation through pressure relief and permeability enhancement, thereby ensuring efficient geothermal energy recovery. The successful application of this system fundamentally depends on a comprehensive understanding of the stress evolution and failure mechanisms within the coal measure strata floor under MD-EU coupling conditions.

3. Theoretical Analysis

As a case study located in the eastern mining area of the Pingdingshan coalfield, Pingdingshan No. 10 Mine rests upon a Cambrian limestone karst heat reservoir. The main coal seam, with an average thickness of 4 m at a depth of 800–1000 m, is notably underlain by a pressurized (>4 MPa) karst aquifer with temperatures of 50–60 °C, located just 80–100 m below. This unique geothermal setting presents a significant opportunity for the SECGR technology but also introduces critical challenges regarding floor stability. This research therefore aims to explore the theoretical stress evolution and failure characteristics of the coal seam floor under MD-EU coupling, with a multi-field coupling mechanical model established for this purpose (Figure 4).

To enable effective analysis of the stress evolution and failure behavior of the coal seam floor under the noted conditions, the original multi-field coupled 3D mechanical model of the mine rock mass (Figure 4) was simplified into a 2D hydraulic model representative of the MD-EU coupling scenario.

Then, the stress evolution law and failure characteristics of coal floor were theoretically analyzed.

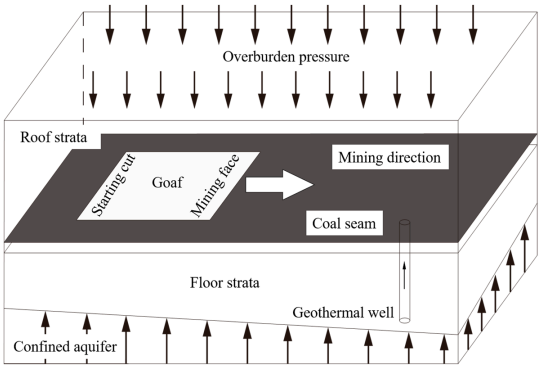


Figure 4. Engineering geological model in Pingdingshan No. 10 Mine.

3.1. Law of Stress Field Distribution

The implementation of the SECGR technology system in Pingdingshan No. 10 Mine necessitates the integrated operation of coal mining above a confined aquifer and negative-pressure extraction from the karst thermal reservoir. This combined activity induces significant stress redistribution and strata failure within the coal seam floor due to mining, while simultaneously altering subsurface pressure conditions through geothermal fluid withdrawal.

Meanwhile, the extraction of geothermal water results in the unloading of the confined aquifer, which further destructs the coal seam floor. The coal seam floor suffers double damage and destruction under MD-EU coupling. Accordingly, a two-dimensional hydromechanical model under MD-EU coupling was established to characterize the stress evolution and identify the failure characteristics of the coal seam floor during the implementation of the SECGR technology.

The distribution of upper load and confined water pressure on the floor rock mass along the strike and dip are presented in Figures 5 and 6 where I and VI are the undisturbed regions with a stress value of γH; II, VI, VII and VIII, which are located in the vicinity of the mining face and the open-off cut, are the stress concentrated regions with stress values of $K_1\gamma H$ and $K_2\gamma H$; III and IX are the pressure relief regions formed by roof caving; V is the confined water action region.

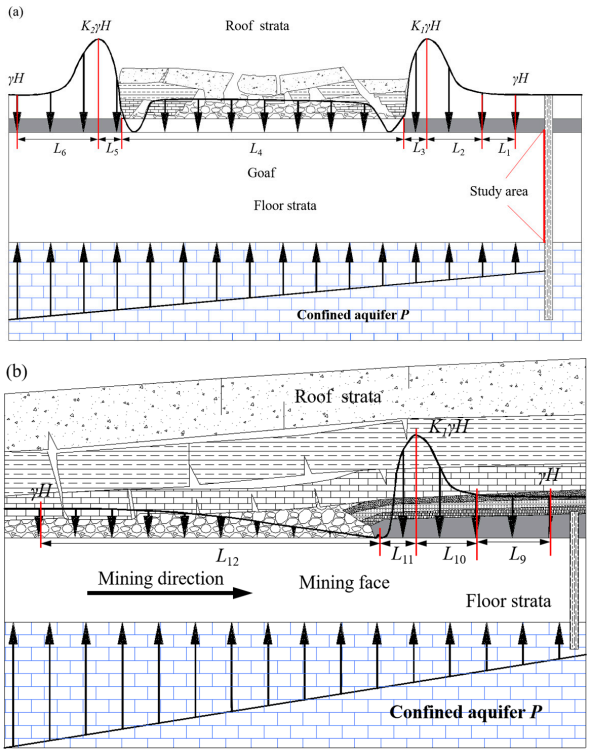


Figure 5. Schematic diagram of stress distribution in coal measure strata under MD-EU coupling: (**a**) along the dip; (**b**) along the strike.

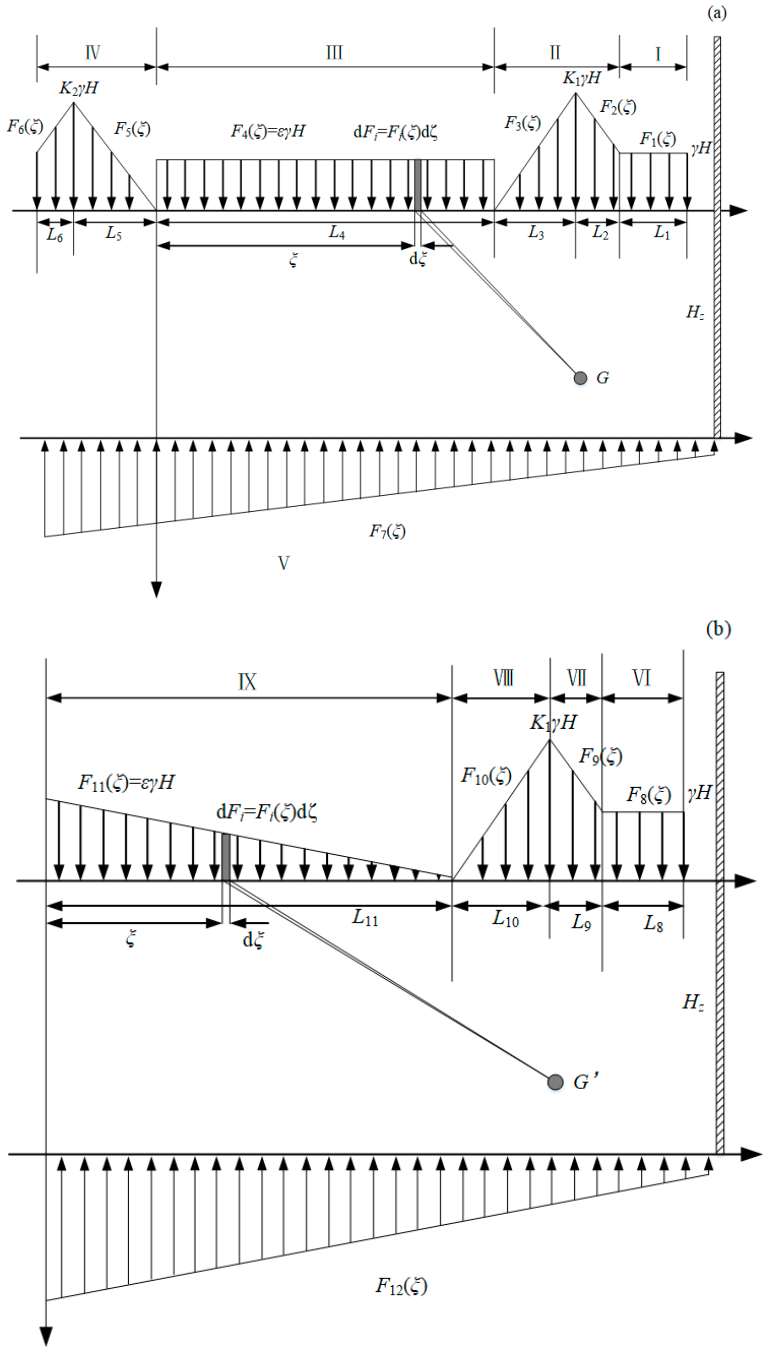


Figure 6. Two-dimensional hydraulic-mechanical (HM) calculation models: (**a**) along the dip; (**b**) along the strike.

Figure 5 depicts the stress distribution within the coal seam floor resulting from the combined influence of mining-induced stress and confined aquifer pressure. For computational analysis, this distribution has been simplified based on the theory of elasticity, employing a linearly distributed equivalent load governing the mechanical behavior.

As displayed in Figure 6, the high water pressure generated by the floor confined water is another important mechanical source leading to the floor failure, and the unloading effect caused by confined water extraction also further aggravates the floor failure. Meanwhile, in the process of confined water extraction, the assumption that the hydraulic gradient phenomenon occurs in the study area is made.

According to the above 2D HM calculation models (Figure 6), a mechanical Equation (1) was established to study the stress distribution state at any points G and G′ of coal seam floor under MD-EU coupling.

The detailed expressions of all loads in Figure 6 are listed as Equation (1) [37,38]:

The detailed expressions for all loads depicted in Figure 6 are provided in Equation (1) [37,38].

$$\begin{array}{ll}
F_1(\xi) = \gamma H & (L_2 + L_3 + L_4 \le \xi \le L_1 + L_2 + L_3 + L_4) \\
F_2(\xi) = \frac{(K_1-1)[(L_2+L_3+L_4-\xi)]\gamma H}{L_2} & (L_3 + L_4 \le \xi \le L_2 + L_3 + L_4) \\
F_3(\xi) = \frac{(\xi-L_4)K_1\gamma H}{L_3} & (L_4 \le \xi \le L_3 + L_4) \\
F_4(\xi) = \varepsilon\gamma H & (0 \le \xi \le L_4) \\
F_5(\xi) = \frac{-K_2\varepsilon\gamma H}{L_5} & (-L_5 \le \xi \le 0) \\
F_6(\xi) = \frac{(K_2-1)[(L_5+L_6+\xi)+L_6]\gamma H}{L_6} & (-L_5 - L_6 \le \xi \le -L_5) \\
F_7(\xi) = -\frac{(L_7+L_8-\xi)}{L_7}P & (L_8 \le \xi \le L_8 + L_7) \\
F_8(\xi) = \gamma H & (L_9 + L_{10} + L_{11} \le \xi \le L_8 + L_9 + L_{10} + L_{11}) \\
F_9(\xi) = \frac{(K_1-1)[(L_{11}+L_{10}+L_9-\xi)]\gamma H}{L_9} & (L_{10} + L_{11} \le \xi \le L_9 + L_{10} + L_{11}) \\
F_{10}(\xi) = \frac{(\xi-L_{11})K_1\gamma H}{L_{10}} & (L_{11} \le \xi \le L_{11} + L_{10}) \\
F_{11}(\xi) = \frac{K_1\gamma H(L_{11}-\xi)}{L_{11}} & (0 \le \xi \le L_{11}) \\
F_{12}(\xi) = \frac{(L_8+L_9+L_{10}+L_{11}-\xi)}{(L_8+L_9+L_{10}+L_{11})}P & (0 \le \xi \le L_8 + L_9 + L_{10} + L_{11})
\end{array} \quad (1)$$

where

γ is the average bulk density of rock in the floor;

H is the average depth of coal seam mining;

P is the water pressure of the aquifer;

ε is the compaction rate of the goaf;

K_1 is the bearing pressure coefficient in front of the strike coal wall;

K_2 is the bearing pressure coefficient of the dip coal walls on both sides;

L_2, L_3, L_5 and L_6 are the lengths of plastic zones on both sides of the working face, m;

L_4 is the length of the working face, m;

L_7 is the length of the confined water unloading zone, m;

L_9, L_{10} and L_{11} are the lengths of the plastic zone, the elastic zone and the stress reduction zone along the working face, m. The specific parameters are shown in Table 1.

Table 1. Theoretical Parameter Annotation Table.

Parameter	Annotation
γ	Average density of basement rocks, kg/m^3.
H	Average mining depth of coal seam, m.
P	Pressure of confined water, MPa.
ε	Gob compaction rate.
K_1	Strike-direction coal wall bearing pressure coefficient.
K_2	Bearing pressure coefficient of the two-side inclined coal walls.
L_2, L_3, L_5 and L_6	Length of the plastic zones on both sides of the working face, m.
L_4	Working face length, m.
L_7	Length of the unloading zone in the geothermal reservoir, m.
L_9	Length of the strike-direction plastic zone at the working face, m.
L_{10}	Length of the strike-direction elastic zone at the working face, m.
L_{11}	Length of the strike-direction stress-relief zone at the working face, m.

A microelement $d\xi$ that is ξ away from the coordinate origin O is taken. Then, the concentrated force here can be expressed as $dF_i = F_i(\xi)d\xi$. Furthermore, the dF_i-induced micro-stress component $G(x,z)$ is:

$$\left.\begin{aligned} d\sigma_z^{(i)} &= -\frac{2F_i(\xi)d\xi}{\pi}\frac{z^3}{\left[z^2+(x-\xi)^2\right]^2} \\ d\sigma_x^{(i)} &= -\frac{2F_i(\xi)d\xi}{\pi}\frac{z(x-\xi)^2}{\left[z^2+(x-\xi)^2\right]^2} \\ d\tau_{zx}^{(i)} &= -\frac{2F_i(\xi)d\xi}{\pi}\frac{z^2(x-\xi)}{\left[z^2+(x-\xi)^2\right]^2} \end{aligned}\right\} \tag{2}$$

In Equations (1) and (2), x-ξ and z represent the horizontal and vertical distances from dF or dF' to G (x, z), respectively.

By transforming Equation (2) from $\xi = \xi_{i1}$ to $\xi = \xi_{i2}$, Equation (3) is defined:

$$\left.\begin{aligned} \sigma_z^{(i)} &= -\frac{2}{\pi}\int_{i1}^{i2}\frac{F_i(\xi)z^3}{\left[z^2+(x-\xi)^2\right]^2}d\xi \\ \sigma_x^{(i)} &= -\frac{2}{\pi}\int_{i1}^{i2}\frac{F_i(\xi)z(x-\xi)^2}{\left[z^2+(x-\xi)^2\right]^2}d\xi \\ \tau_{zx}^{(i)} &= \int_{i1}^{i2}\frac{F_i(\xi)z^2(x-\xi)}{\left[z^2+(x-\xi)^2\right]^2}d\xi \end{aligned}\right\} \tag{3}$$

Based on the strike stress (σ_{z1},σ_{x1} and τ_{zx1}) and dip stress (σ_{z2},σ_{x2} and τ_{zx2}), the total stress components (σ_z, σ_x and τ_{zx}) can be calculated as follows:

$$\left.\begin{aligned} \sigma_{z1} &= \sum_{i=1}^{8}\sigma_z^{(i)} \\ \sigma_{x1} &= \sum_{i=1}^{8}\sigma_x^{(i)} \\ \tau_{zx1} &= \sum_{i=1}^{8}\tau_{zx}^{(i)} \end{aligned}\right\} \tag{4}$$

$$\left.\begin{aligned} \sigma_{z2} &= \sum_{i=9}^{13}\sigma_z^{(i)} \\ \sigma_{x2} &= \sum_{i=9}^{13}\sigma_x^{(i)} \\ \tau_{zx2} &= \sum_{i=9}^{13}\tau_{zx}^{(i)} \end{aligned}\right\} \tag{5}$$

3.2. Calculation of Failure Depth

The recovery of the working face induces strata movement, primarily resulting in shear deformation within the floor. According to the theory of elasticity, failure occurs when the maximum shear stress at any point exceeds the material's shear strength. Consequently, based on this premise and the predominance of shear failure, the Mohr-Coulomb criterion is adopted. Equation (6) is thus established to calculate the extent of floor failure, defining the failure criterion as being governed by the shear strength of the rock mass [17,39]:

$$F(x,z) = \frac{\frac{\sigma_z+\sigma_x}{2}\tan\varphi + c}{\sqrt{\tan^2\varphi + 1}} - \tau_{\max} \tag{6}$$

In the previous section, the solution formula of stress component of stope floor under MD-EU coupling in the SECGR technology system has been calculated in the light of the

theory of elasticity, and the stress distribution law of floor under unloading action has been explored. To determine the failure depth of the floor, analysis was conducted employing the Mohr-Coulomb criterion, which governs shear failure. Accordingly, the maximum shear stress at any arbitrary point G within the floor can be expressed as:

$$\tau_{\max} = \sqrt{\tau_{zx}^2 + \left(\frac{\sigma_z - \sigma_x}{2}\right)^2} \tag{7}$$

The constructed function Equation (6) represents the difference between the shear strength and the maximum shear stress, and the rock mass will be destroyed when $F(x,z) \leq 0$.

4. Numerical Methods and Materials

4.1. Methods and Materials

Under MD-EU coupling, the coal seam floor (thermal storage cover) changes from an intact state to an unloading state, which conduces to high-pressure confined water seepage and inrush. To observe the floor failure characteristics under mining-seepage conditions in detail, the fluid–solid coupling module in Flac3D 6.0 software was used to conduct numerical simulation on the coupling effect of mining disturbance and extraction unloading.

Taking the geological column of Pingdingshan No. 10 Mine as the design principle, the numerical model was established through the fluid–solid coupling module in Flac3D 6.0 software. A numerical model with dimensions of 200 m in length, 250 m in width, and 140 m in height was established, employing the Mohr-Coulomb constitutive model to represent the mechanical behavior of the rock mass, as illustrated in Figure 7.

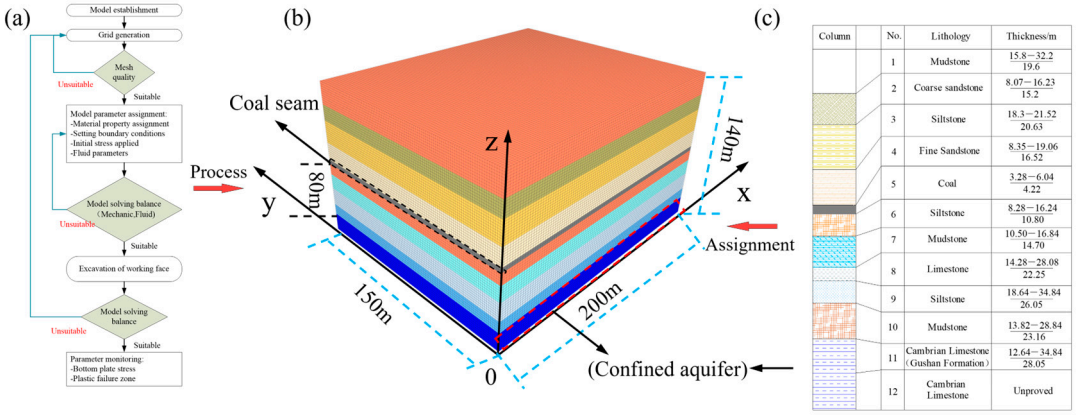


Figure 7. Diagram of numerical simulation model. (**a**) Simulated flowchart (**b**) Numerical model diagram. (**c**) Geological histogram.

The bottom boundary of the model was set as a fixed constraint; the equivalent vertical load of 20 MPa was applied to the top to simulate the in situ stress caused by all overburden layers; and other boundaries, whose horizontal displacement was constrained, were set as impermeable boundaries. The pore water pressure of 4 MPa was applied in the confined water layer, and it was set to decrease stepwise in X and Y directions to simulate the change in pore water pressure in the confined water layer during geothermal water extraction. This study employs the automatic time-stepping algorithm built into FLAC3D 6.0 (activated by the command "SET ffauto on") to address numerical stability in the hydro-mechanical coupling calculations. The impact of mining disturbance on the floor was simulated through a stepwise excavation approach.

The continuum models were analyzed by hydromechanical coupling to characterize floor damage and flow during the mining of coal and the depressurization extraction

of karst heat storage. The calculations concerning failure were all guided by the Mohr-Coulomb criterion. The values of rock mechanics parameters in Table 2 were empirically determined with reference to the literature. The parameters listed in Table 2 were primarily synthesized from published studies [40,41] conducted under geological conditions similar to those of the region investigated in this work. These literature sources derived typical parameter ranges through laboratory tests and in situ water pressure tests.

Table 2. Rock mechanics parameters [40,41].

Lithology	Density/ ($kN \cdot m^{-3}$)	Bulk Modulus/ GPa	Shear Modulus/ GPa	Cohesion/ MPa	Friction Angle/ (°)	Tensile Strength/ MPa	Permeability/ ($m^2 \cdot (Pa \cdot s)^{-1}$)	Porosity
Mudstone	25	5.0	3.2	4.0	32	3.0	6×10^{-15}	0.3
Coarse sandstone	28	6.2	2.8	5.5	32	3.2	6×10^{-15}	0.2
Siltstone	25	6.0	4.1	5.0	33	2.8	7×10^{-15}	0.2
Fine sandstone	23	4.8	3.6	4.6	35	3.0	6.5×10^{-15}	0.3
Coal seam	13.9	2.3	2.0	2.1	20	1.1	3×10^{-13}	0.4
Confined aquifer	24	4.0	2.3	2.0	31	2.1	4×10^{-10}	0.7

4.2. Principles of Hydro-Mechanical Coupling

(1) Fluid Flow Equation (Darcy's Law)

Fluid flow in the porous medium is fully described by Darcy's law. The governing equation in differential form is expressed as:

$$q = -k\nabla p \tag{8}$$

where q is the Darcy velocity (or specific discharge), k is the permeability coefficient (related to the intrinsic permeability), and ∇p is the pore pressure gradient.

This equation is embedded within the fluid computation module of FLAC3D 3.0 and is utilized to calculate fluid flow through the porous medium.

(2) Equilibrium Equation

The mechanical response of the system is governed by the stress equilibrium equation:

$$\nabla\sigma + \rho_{tot} g = 0 \tag{9}$$

where σ is the total stress tensor, ρ_{tot} is the bulk density of the saturated medium, and g is the gravitational acceleration vector.

(3) Coupling Mechanism

A full two-way coupling between the solid and fluid phases is implemented through the following physical interactions:

Solid-to-Fluid Influence: Changes in the elemental volume induce variations in pore pressure. This mechanism is numerically implemented in FLAC3D 6.0 via the fluid bulk modulus and the evolution of porosity.

Fluid-to-Solid Influence (Effective Stress Principle): Fluctuations in pore pressure (p) fundamentally alter the mechanical response of the solid skeleton. This critical interaction is governed by the effective stress principle, expressed as $\sigma' = \sigma - p$, where σ' represents the effective stress that actually controls material deformation and failure. Consequently, the constitutive model of the material (e.g., Mohr-Coulomb plasticity) is formulated and computed based on this effective stress (σ'), rather than the total stress (σ).

5. Results

Based on the data processing module developed in Python, the vertical, horizontal, and shear stresses at any point within the coal seam floor under MD-EU coupling conditions were systematically calculated using Equations (1)–(5), with corresponding stress nephograms generated to visualize the distribution. Subsequently, the failure depths along both the strike and dip directions of the coal seam were determined by applying the floor failure criterion given in Equation (6). The reliability of the theoretical calculations was further validated by comparing them with numerically simulated failure characteristics and the evolution of the plastic zone during stepwise excavation. Together, these analyses provide a valuable reference for assessing the hydraulic failure behavior of coal seam floors under MD-EU coupling.

5.1. Map of Floor Stress Distribution

Figure 8 illustrates the vertical stress distribution in the coal seam floor along the strike and dip directions under MD-EU coupling. The distribution is characterized by distinct stress concentration and release areas, a pattern primarily induced by variations in upper abutment pressure. Specifically, the concentration zone, correlating with high abutment pressure, is located beneath the coal pillar, whereas the release area underlies the goaf. The peak vertical stress reaches 23.7 MPa along the strike, while along the dip, the peak values of 14.3 MPa and 25.2 MPa are identified at the elastic-plastic boundary of the coal seam.

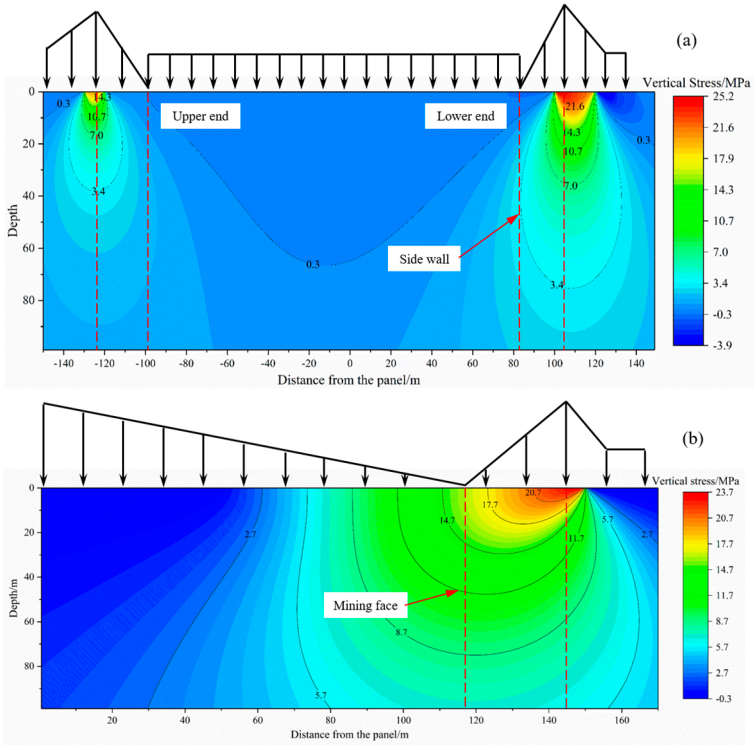


Figure 8. Map of vertical stress distribution of the coal seam floor under MD-EU coupling: (**a**) along the dip; (**b**) along the strike.

Along the dip of the coal seam floor, the vertical stress is obviously asymmetrically distributed, especially in the area with a strong unloading effect. Its value decreases nonlinearly at a decelerating rate with the increase in buried depth. The main reason is that the bearing capacity of karst thermal storage weakens after unloading, which leads to the expansion of the coal seam floor. Furthermore, mining disturbance exacerbates the nonlinear damage accumulation within the floor strata, thereby facilitating a deeper propagation of vertical stress.

Thus, the asymmetric site of floor stress along the dip of the working face is caused by coupling of dynamic disturbance and extraction unloading. In addition, compared with the floor stress distribution map in the literature [42,43], the stress distribution of the coal seam floor is still mainly affected by mining disturbance.

Figure 9 shows the horizontal stress distribution map of the coal seam floor under MD-EU coupling along the working face. As can be observed from Figure 9, compared with vertical stress redistribution which causes obvious division of the stress concentration area and the release area, horizontal stress redistribution is relatively gentle, and the stress concentration is obviously weakened and mainly occurs within the range of 18 m of the coal seam floor. Below 60 m in the vertical direction, the horizontal stress changes gently or even ceases changing, which indicates that the influence range of horizontal stress shrinks rapidly with the increase in floor depth. Hence, it can be inferred that the continuously distributed normal load induces the generation of both vertical stress and horizontal stress, but the influence range of horizontal stress on the floor is small. This inference is consistent with the computational procedure of Equation (3), which accounts for the relatively minor influence of the vertical distance (z) between any point in the floor and the coal seam on the magnitude of horizontal stress.

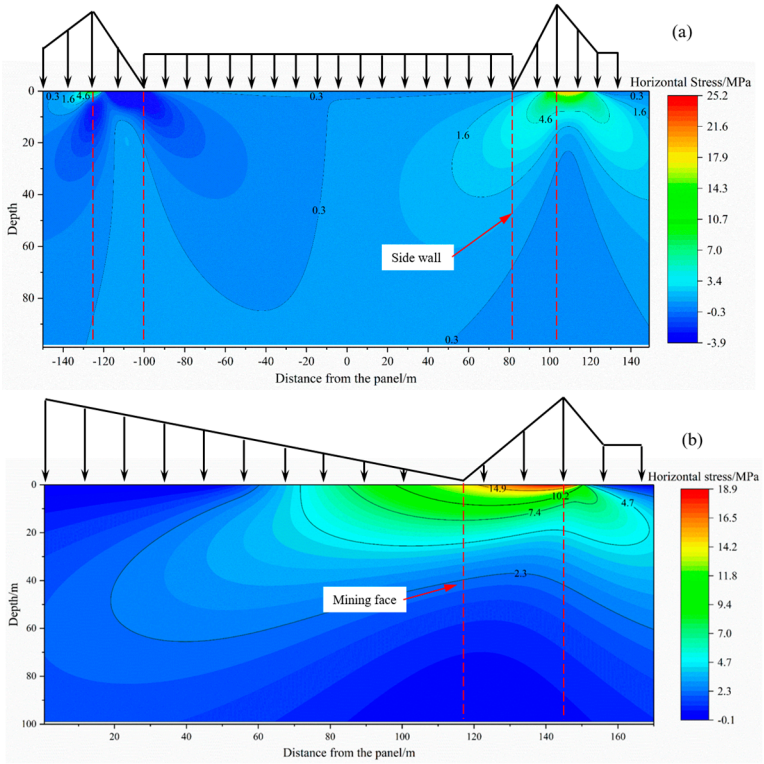


Figure 9. Map of horizontal stress distribution of the coal seam floor under MD-EU coupling: (**a**) along the dip; (**b**) along the strike.

Finally, according to the isoline of horizontal stress distribution map, the unloading effect produced by decompression extraction of karst heat storage is an important factor affecting the distribution range of horizontal stress. The more obvious its effect is, the wider the distribution range of horizontal stress and the more obvious its diffusion are. And the degree of stress diffusion and attenuation also rises with the increase in unloading effect.

Figure 10 shows the shear stress distribution map of the coal seam floor along the dip and strike of the working face under MD-EU coupling. Clearly, the maximum shear stress occurs at the load edge. In Figure 10a, the shear stress presents a saddle-shaped distribution between the peak values of the load stress, which is basically symmetrical along the vertical

line of the working face, and the shear stresses at both ends obliquely propagate downward at a certain angle with the normal direction of the floor. A positive and negative shear couple occurs in the underlying rock layer corresponding to the load edge area, which makes the floor rock mass more prone to compression-shear or tension-shear deformation and failure. From Figure 10a, stress concentration occurs in the underlying rock mass at both ends of the working face, and the maximum shear stresses are basically equal, about 1.3 MPa. Despite the small value of peak stress in the shear stress concentration area, its influence range is broader, indicating that the vertical stress of the floor under unloading aggravates floor deformation and expansion, which leads to an obvious increase in the range of shear stress. However, the expansion and deformation of rock mass reduce the stress concentration value of shear stress. Shear yield easily occurs in shear stress concertation areas in the coal seam floor, resulting in the development of shear cracks and the formation of water channels. Therefore, it is necessary to pay attention to the water level change in the shear stress concertation areas in the floor during coal mine production.

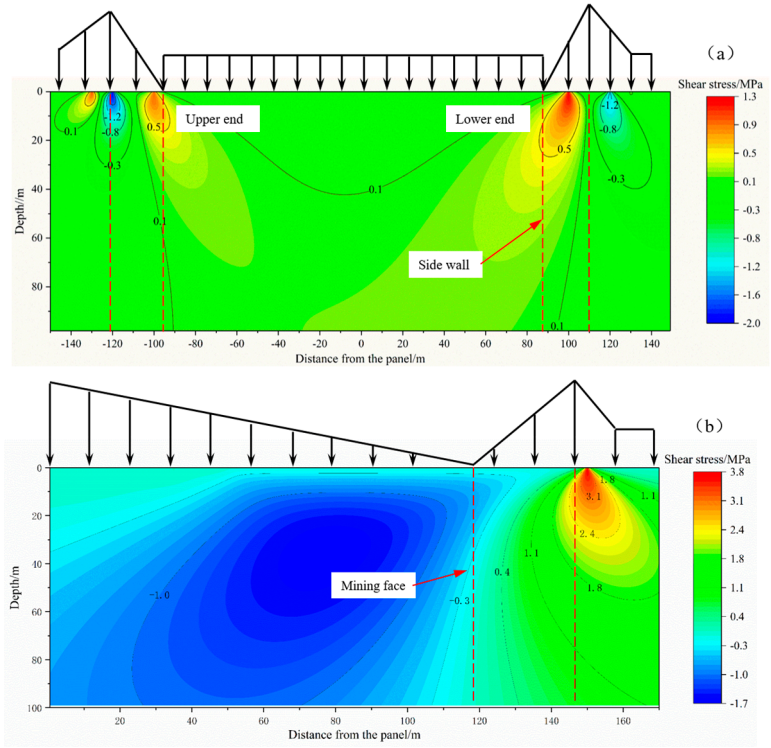


Figure 10. Map of shear stress distribution of the coal seam floor under MD-EU coupling: (**a**) along the dip; (**b**) along the strike.

5.2. Map of Floor Failure Depth

Using Python 3.11 and Origin 2024 software, the theoretical failure modes of the stope floor along the dip and strike of the working face were obtained by substituting relevant parameters (Figure 4). The contour maps in the figure were obtained by the above formulas, and the parts where the depth is smaller than 0 represent the failure of floor rock mass. Figure 4 presents the contour plot of floor failure derived from Equation (7). Based on the calculation results of this equation, failure is considered to occur where the maximum shear stress τmax falls below zero. Using the criterion τmax = 0, we have delineated the preliminary failure boundary of the floor, as indicated by the dashed line in Figure 4.

Figure 11 shows failure depth distribution of the coal seam floor along the strike and dip of the working face under MD-EU coupling. According to Figure 11, under MD-EU coupling, the failure mode of the floor resembles that of the shear stress distribution area, and the failure mode along the strike can be divided into two parts. Specifically, the failure

mode beyond 80 m behind the working face tends to be stable and straight, while that from 80 m behind the working face to 50 m in front of the working face presents an inverted-S shape. The failure mode along the dip presents an approximately inverted-saddle shape, which agrees with the failure mode of the floor obtained by Song [39,42]. Along the strike, the maximum failure depth of the floor in front of the coal wall is about 45 m, and the failure tends to further develop downwards; additionally, the failure depth of the floor behind the working face is about 20 m. Along the dip of the working face, the maximum failure depth is 28 m, and a failure mode that is deep at both ends and shallow in the middle is formed. The reason is that the areas near the coal pillars at both ends undergo heavy stress concentration and witness the appearance of shear force couples; consequently, the failures easily occur from both ends gradually expand and extend to the floor of the central goaf and connect with each other. In addition, the shear failure depth of the floor is large within the range of peak abutment pressure, but it is relatively small in the pressure relief section of the goaf. In summary, extraction unloading caused by negative-pressure extraction of karst heat storage leads to the uneven failure depth of the floor, and the failure depth is larger in the areas with strong extraction unloading, which is consistent with the unloading effect on shear stress.

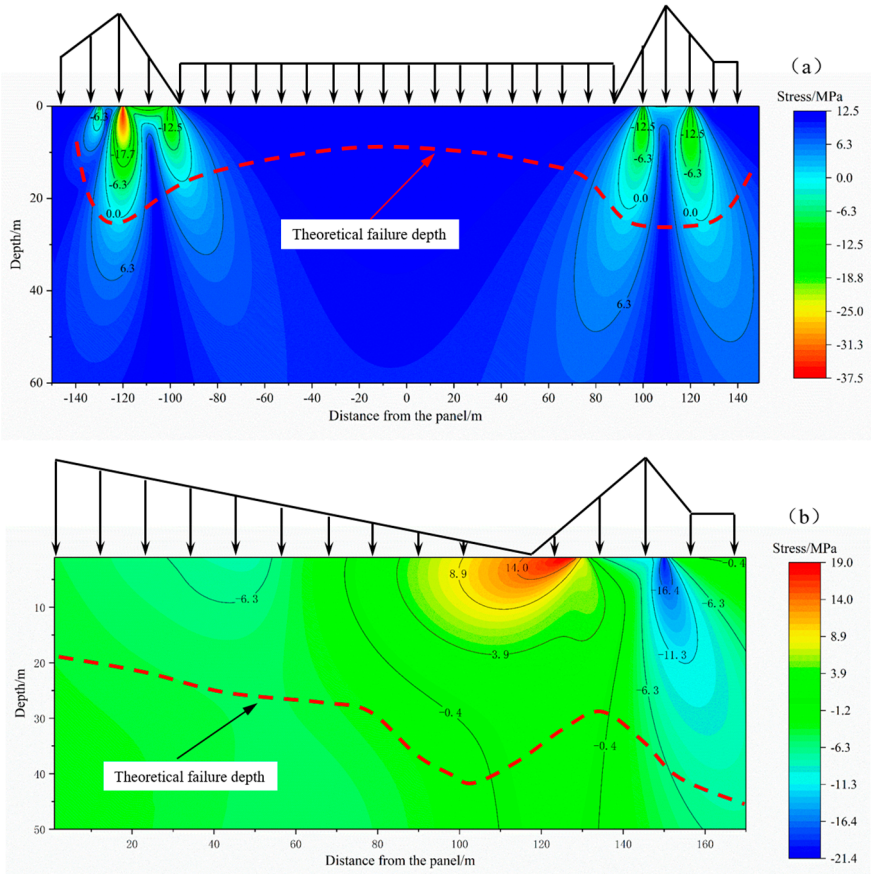


Figure 11. Map of shear stress distribution of the coal seam floor under MD-EU coupling: (**a**) along the dip; (**b**) along the strike.

A comparison with existing literature reveals that the computational results from the hydro-mechanical coupling model established in this study are generally consistent with the floor stress model developed by Song et al. in terms of both stress distribution patterns and magnitude. This consistency in observed behavior supports the rationality of the assumptions and parameters adopted in our work, thereby providing a foundational basis for our numerical simulations.

5.3. Map of the Floor Plastic Zone Along the Strike

Generally speaking, the coal seam floor experiences stress redistribution under MD-EU coupling, which induces different degrees of unloading damage to it. However, the unloading effect caused by decompression extraction of karst heat storage is mainly reflected in the non-uniform regional damage caused by unloading of confined water and its overlying strata. Figure 12 shows the relationship between the floor failure depth, the development area of the plastic zone above confined water and the advancement distance of the working face during numerical simulation.

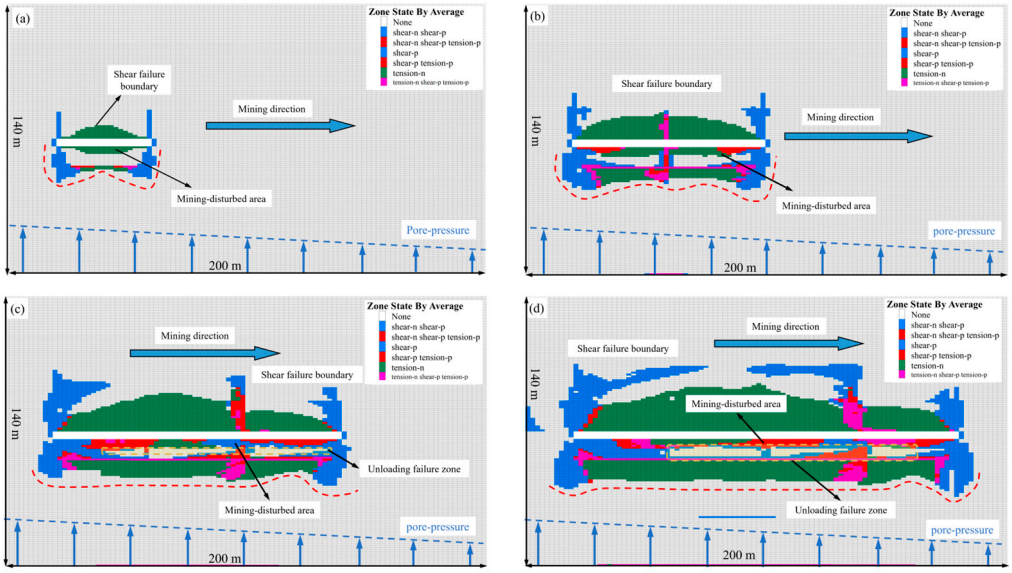


Figure 12. Map of shear stress distribution of the coal seam floor under MD-EU coupling: (**a**) mining distance, 50 m; (**b**) mining distance, 100 m; (**c**) mining distance, 150 m; (**d**) mining distance, 200 m.

Figure 12 shows the floor plastic zone along the strike at different mining distances under MD-EU coupling. As exhibited Figure 13, in the early stage of mining, the floor is barely affected by MD-EU coupling, and the failure zone is almost symmetrically distributed in the shape of an inverted saddle. The predominance of shear failure suggests that the effective aquiclude between the confined aquifer and the coal seam remains sufficiently thick at this stage, while the extraction-induced unloading from karst thermal reservoir depressurization has only a marginal influence on the floor failure depth.

With the continuous advancement of the working face, the floor failure depth gradually increases, and the failure continuously moves forward, while the plastic zone expands downwards in an asymmetric manner. It can be seen from the failure state that under MD-EU coupling, the floor below the working face mainly undergoes shear failure, while the rock mass lying under the goaf primarily experiences tensile failure. This corresponds to the position of the shear couple in Figure 10a. Moreover, the final failure mode of the coal seam floor resembles the theoretical calculation results, the inverted-S-shaped failure mode near the working face. Therefore, the unloading effect caused by decompression extraction of karst heat storage further aggravates the floor failure, and the distribution of plastic zone coincides with the theoretical calculation results; additionally, the plasticity develops vigorously in areas with a strong unloading effect.

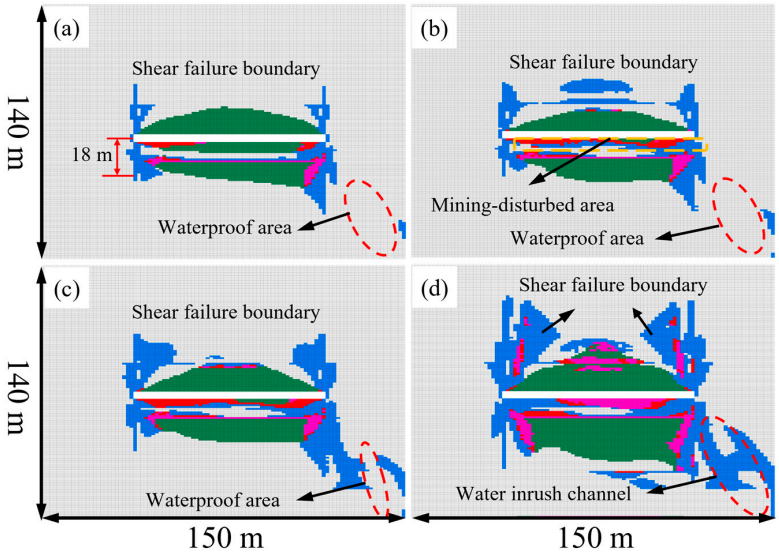


Figure 13. Map of the floor plastic zone along the dip under MD-EU coupling: (**a**) mining distance, 50 m; (**b**) mining distance, 100 m; (**c**) mining distance, 150 m; (**d**) mining distance, 200 m.

5.4. Map of the Floor Plastic Zone Along the Dip

Figure 13 depicts the evolution of the plastic zone along the floor's dip direction under extraction-induced unloading. As illustrated, the failure process evolves through four distinct stages: the undisturbed stage, crack initiation stage, crack development stage, and finally, crack coalescence stage. Analysis indicates that as the working face advances, floor failure progressively extends from both ends toward the center. The ultimate failure mode, characterized predominantly by shear failure with a depth range of 18–46 m, demonstrates strong agreement with both theoretical calculations and previous research findings by Liang et al. [39,43].

Meanwhile, three distinct characteristic zones are identified within the floor rock mass: the mining-induced failure zone, the intact aquiclude (complete rock stratum), and the unloading-activated zone.

Once the discrete cracks under high confined water pressure are hydraulically connected with the mining failure area, a large amount of groundwater will enter the roadway uncontrollably, thus causing water inrush accidents. In Figure 13, the maximum failure depth and the shear-couple-induced tensile-shear damage zone appear in the unloading zone of decompression extraction of karst heat storage. Based on the above results, the numerical simulation results basically agree with the theoretical calculation results, and the calculation results can provide theoretical explanation for the field application of the SECGR technology system.

6. Discussion

Based on the integrated theoretical and numerical simulation results presented above, the MD-EU coupling mechanism significantly governs the stress evolution and failure characteristics of the coal seam floor.

The essence of their effect on the floor rock mass is to induce unloading failure of the rock mass. As disclosed in the research of Zhao et al. [44,45], the two key factors of unloading failure are unloading stress and unloading time. Among them, unloading stress is mainly reflected in the mining disturbance intensity of the working face and the unloading effect of high-pressure confined water, while unloading time is mainly manifested in the speed of working face advancement and the speed of karst heat storage depressurization extraction. Specifically, faster working face advancement and karst heat

storage depressurization extraction correspond to a higher unloading speed and a shorter unloading time of rock mass. To ensure safe and economic implementation of the SECGR technology system, this study focuses on the influences of working face advancement and karst heat storage depressurization extraction speeds (unloading time) on the failure characteristics of stope floor rock mass. Furthermore, it also aims to explore more factors influencing the failure characteristics. Such a study is valuable in engineering applications. In view of the above fact, the deformation and failure of stope floor rock mass under the influences of working face advancement and karst heat storage depressurization extraction speeds (unloading time) are analyzed and discussed in this section.

Unloading induces rebound deformation in the rock mass along the unloading direction. As described by the constitutive relation of rock mass, this deformation generates tensile stress in the same direction. Thus, the MD-EU coupling effectively superimposes a reverse tensile stress onto the pre-existing stress field. By defining the unloading stresses along the maximum and minimum principal stresses as $\Delta\sigma_1$ and $\Delta\sigma_3$, respectively, the resultant stresses under MD-EU coupling become $(\sigma - \Delta\sigma_1)$ and $(\sigma - \Delta\sigma_3)$. The corresponding stress decomposition is illustrated in Figure 14.

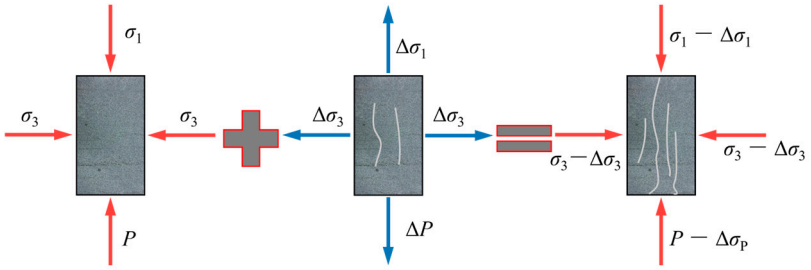


Figure 14. Diagram of unloading stress decomposition.

In the unloading process, the relationship between the damage factor D of rock mass, unloading stress $\Delta\sigma$ and unloading time T $(T_1 + T_2)$ is assumed as follows:

$$D = 1 - (a_0\Delta\sigma)^{-b_0(T_1+T_2)} \tag{10}$$

where a_0 and b_0 are rock mass parameters, respectively; T_1 indirectly represents the speed of working face advancement; and T_2 indirectly represents the speed of confined water extraction. The faster the working face advancement and confined water extraction, the smaller the unloading times T_1 and T_2, $T = T_1 + T_2$.

According to Lemaitre's principle of strain equivalence [46], the constitutive relation of damaged material $(D \neq 0)$ can be deduced from the constitutive relation of nondestructive material $(D = 0)$. In the process of derivation, the effective stress tensor of damaged material $\widetilde{\sigma}$ can be substituted for that of lossless material σ. The relation between effective stress tensor $\widetilde{\sigma}$ and σ can be expressed as follows:

$$\widetilde{\sigma} = \sigma \cdot (I - D)^{-1} \tag{11}$$

where I is the unit tensor.

The creep equation in the 1D Burgers model [47] is developed into a 3D one by analogy. where $\varepsilon(t)$ is the total axial strain; K is the bulk modulus, GPa; G_1 and G_2 are shear moduli; η_1 and η_2 are the viscosity coefficients, $GPa \cdot h$. For the convenience of analysis, it is

assumed that the confining pressure of rock mass is equal, that is $\sigma_2 = \sigma_3$, and σ is replaced with $\widetilde{\sigma}$. In this way, the creep equation is simplified as:

$$\varepsilon(t) = \frac{1}{9K}(\widetilde{\sigma}_1 + 2\widetilde{\sigma}_3) + \frac{\widetilde{\sigma}_1 - \widetilde{\sigma}_3}{3G_1} + \frac{\widetilde{\sigma}_1 - \widetilde{\sigma}_3}{3\eta_1}(t) + \frac{\widetilde{\sigma}_1 - \widetilde{\sigma}_3}{3G_2}\left[1 - \exp\left(-\frac{G_2}{\eta_2}t\right)\right] \quad (12)$$

By substituting Equations (10) and (11) into Equation (12), the creep constitutive equation considering unloading stress and unloading time is obtained as follows (Table 3):

$$\varepsilon(t) = \frac{1}{9K}\left(\frac{\Delta\sigma_1}{\zeta_1(a_0\Delta\sigma_1)^{-b_0(T_1+T_2)}} + \frac{2\Delta\sigma_3}{\zeta_3(a_0\Delta\sigma_3)^{-b_0(T_1+T_2)}}\right) + \frac{1}{2}\left(\frac{\Delta\sigma_1}{\zeta_1(a_0\Delta\sigma_1)^{-b_0(T_1+T_2)}} - \frac{2\Delta\sigma_3}{\zeta_3(a_0\Delta\sigma_3)^{-b_0(T_1+T_2)}}\right)\cdot\left[\frac{1}{G_1} + \frac{(T_1+T_2)}{\eta_1} + \frac{1}{G_2}\left(1 - \exp\left(-\frac{G_2}{\eta_2}t\right)\right)\right] \quad (13)$$

Table 3. Model calculation parameters [48].

$\Delta\sigma_1$/MPa	ζ_1/%	$\Delta\sigma_3$/MPa	ζ_3/%	a_0	b_0	G_1/GPa	G_2/GPa	η_1/(Gpa·h)	η_2/(Gpa·h)
38	0.75	32	0.585	0.04	0.25	2480	17,496	486,862	526,738

Based on the mechanical parameters of floor rock mass and the different unloading times (T_1 + T_2) in the paper, the creep law of rock mass was obtained (Figure 15). As illustrated in Figure 15, the unloading rate (working face advancement and karst heat storage depressurization extraction speeds) has a considerable influence on the failure degree of rock mass. The faster the working face advancement and karst heat storage depressurization extraction (the smaller T_1 + T_2), the more severe the deformation of rock mass and the higher its damage degree. In the initial stage of mining, the failure degree of rock mass increases linearly. After MD-EU coupling for a certain time, the failure degree tends to flatten, no longer increasing or just increasing slowly. This theoretically shows that proper control of working face advancement and karst heat storage depressurization extraction speeds can effectively slow down the failure speed of floor rock mass. Moreover, the failure degree of the floor has a certain limit, and it will not continue to increase when it exceeds the limit value. However, the actual influence characteristics of working face advancement speed (unloading speed) on the failure mode of floor rock mass need further field verification.

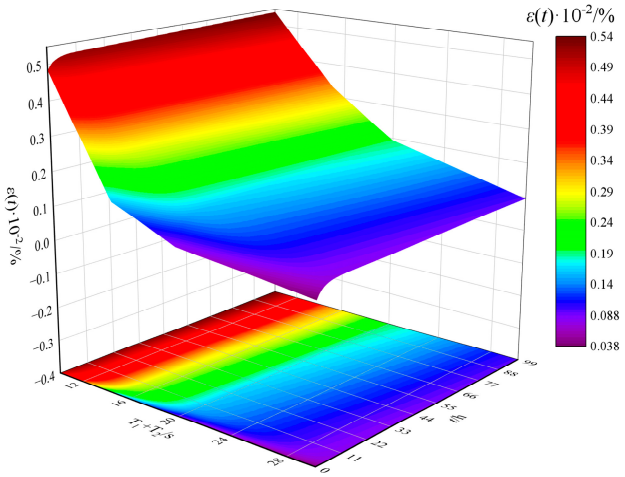


Figure 15. Creep curves of the floor under different unloading times.

7. Conclusions

This study designed and implemented the SECGE system technology based on the engineering background of Pingdingshan No. 10 Mine. This system offers a novel approach

to integrated resource extraction and environmental conservation. A 2D hydraulic calculation model of the floor under MD-EU coupling model was used to investigate stress field distribution patterns and failure mechanisms in the coal seam floor during coal and thermal resource extraction. Numerical simulations further analyzed the dynamic evolution of floor damage characteristics under extraction-induced stresses. Additionally, the Burgers viscoelastic model was applied to quantify time-dependent rock mass damage evolution caused by mining-induced unloading effects. The main conclusions of this study are as follows:

(1) Following multiple tectonic events, certain strata in the Pingdingshan coalfield have been eroded, resulting in an overall uplift structure with a central syncline. This geological framework has given rise to a high geothermal heat flow ranging from 60 to 80 mW/m^2, forming geothermal resources associated with coal measures. These conditions provide a natural foundation for the application of the SECGR technology system.

(2) Under the coupled effects of mining disturbance and extraction unloading (MD-EU), vertical stress exhibits an asymmetric distribution, with mining disturbance being the dominant factor governing stress redistribution. Both the distribution range of horizontal stress and the extent of stress attenuation increase with greater unloading. Shear stress displays a saddle-shaped distribution on the goaf floor, where shear couples induce shear failure. Unloading expands the distribution range of shear stress while reducing its peak magnitude.

(3) The mining-induced failure zones along the strike and dip of the coal seam floor exhibit inverted-S and inverted-saddle shapes, with respective failure depths of 35 m and 28 m, consistent with numerical simulation results. Simulations further indicate that hydraulic unloading induces asymmetric failure in the floor. As mining proceeds, floor failure undergoes four distinct stages: undisturbed, crack initiation, crack development, and crack connection. Additionally, three characteristic zones are identified in the floor rock mass: the mining failure zone, the waterproof zone, and the unloading activation zone.

(4) The Burgers model provides a valid framework for characterizing the relationship between unloading rates and rock mass damage evolution. Based on the creep equation derived from this model, the influence of unloading rate on floor failure mechanisms was analyzed. During initial mining stages, higher unloading rates lead to more severe rock mass damage, showing an approximately linear increase. With continued mining, the extent of rock mass damage eventually stabilizes or increases only marginally.

Author Contributions: All the authors made contributions to this work. J.L.: Writing—original draft, Visualization, Validation, Methodology, Formal analysis, Data curation, Conceptualization; L.X.: Writing—review and editing, Software, Formal analysis; J.M.: Writing—review and editing, Methodology, Data curation; W.C.: Writing—review and editing, Investigation; Z.Z.: Writing—review and editing, Methodology, Data curation; Z.Y.: Writing—review and editing, Supervision; K.Y.: Writing—review and editing. All authors have read and agreed to the published version of the manuscript.

Funding: This research was sponsored by Qing Lan Project of Jiangsu Province and the Zhangjiagang Science, Technology Development Plan of Zhangjiagang Science and Technology Bureau (Grant No. ZKHBZ2439), the Fundamental Research Funds for the Central Universities (Project No.: 2025QN1015) and the China Postdoctoral Science Foundation (Project No.: 2024M763561).

Institutional Review Board Statement: Not applicable.

Informed Consent Statement: Not applicable.

Data Availability Statement: The data presented in this study are available on request from the corresponding author.

Acknowledgments: The authors would like to thank the editors and the anonymous reviewers for their valuable comments and suggestions, which helped to improve the manuscript.

Conflicts of Interest: The authors declare no conflicts of interest.

References

1. Liu, Y.; Wang, G.; Zhu, X.; Li, T. Occurrence of geothermal resources and prospects for exploration and development in China. *Energy Explor. Exploit.* **2021**, *39*, 536–552. [CrossRef]
2. Luo, S.; Hu, W.; Liu, W.; Zhang, Z.; Bai, C.; Huang, Q.; Chen, Z. Study on the decarbonization in China's power sector under the background of carbon neutrality by 2060. *Renew. Sustain. Energy Rev.* **2022**, *166*, 112618. [CrossRef]
3. Al-Qadami, E.H.H.; Mustaffa, Z.; Al-Atroush, M.E. Evaluation of the Pavement Geothermal Energy Harvesting Technologies towards Sustainability and Renewable Energy. *Energies* **2022**, *15*, 1201. [CrossRef]
4. Chudy, K. Mine Water as Geothermal Resource in Nowa Ruda Region (SW Poland). *Water* **2022**, *14*, 136. [CrossRef]
5. Banks, D.; Steven, J.; Black, A.; Naismith, J. Conceptual Modelling of Two Large-Scale Mine Water Geothermal Energy Schemes: Felling, Gateshead, UK. *Int. J. Environ. Res. Public Health* **2022**, *19*, 1643. [CrossRef]
6. Wan, Z.; Bi, S.; Zhang, Y.; Wang, J.; Wu, D.; Wang, J. Framework of the theory and technology for simultaneous extraction of coal and geothermal resources. *J. China Coal Soc.* **2018**, *43*, 2099–2106. [CrossRef]
7. Huang, Q.; Cheng, J. Research on stress distribution and failure characteristics of coal mining floor in soft-hard alternant strata. *J. Rock Soil Mech.* **2017**, *38*, 36–42. [CrossRef]
8. Zhang, Y. Distribution law of floor stress during mining of the upper protective coal seam. *Sci. Prog.* **2020**, *103*, 0036850420930982. [CrossRef]
9. Liu, W.; Meng, X.J.G. Study on the Relationship Among Temperature, Seepage and Stress in the Excavation Process. *Geotech. Geol. Eng.* **2017**, *36*, 377–387.
10. Liu, S.; Liu, W.; Shen, J. Stress evolution law and failure characteristics of mining floor rock mass above confined water. *KSCE J. Civ. Eng.* **2017**, *21*, 2665–2672. [CrossRef]
11. Zhang, S.; Guo, W.; Li, Y. Experimental simulation of water-inrush disaster from the floor of mine and its mechanism investigation. *Arab. J. Geosci.* **2017**, *10*, 503. [CrossRef]
12. He, L.-B.; Hou, B. Floor Destruction Characteristic Study of Confined Water Effected by Mining Conditions. In Proceedings of the 1st International Workshop on Hydraulic Equipment and Support Systems for Mining (IWHEM 2012), Huludao, China, 17–18 August 2012; pp. 253–258.
13. Zhao, B.; Wang, X.-M.; Li, Y.-W.; Zheng, J.-J.; Yao, Z.-Q.; Zhang, Q.-L. Safe Mining Feasibility of Permanent Waterproof Jamb in Kangjiawan Mine. *J. Kunming Univ. Sci. Technol. (Sci. Technol.)* **2009**, *34*, 27–34.
14. Wang, L.G.; Han, M.; Wang, Z.S.; Ou, S.B. Stress distribution and damage law of mining floor. *J. Min. Saf. Eng.* **2013**, *30*, 317–322.
15. Meng, X.R.; Xu, C.H.; Gao, Z.N.; Wang, X.Q. Stress distribution and damage mechanism of mining floor. *J. China Coal Soc.* **2010**, *35*, 1832–1836.
16. Zhu, S.Y.; Jiang, Z.Q.; Yao, P.; Xiao, W.G. Application of Analytic Method in Calculating Floor Stress of a Working Face. *J. Min. Saf. Eng.* **2007**, *24*, 191–194.
17. Song, W.; Liang, Z. Theoretical and numerical investigations on mining-induced fault activation and groundwater outburst of coal seam floor. *Bull. Eng. Geol. Environ.* **2021**, *80*, 5757–5768. [CrossRef]
18. Li, W.; Liu, Y.; Qiao, W.; Zhao, C.; Yang, D.; Guo, Q. An Improved Vulnerability Assessment Model for Floor Water Bursting from a Confined Aquifer Based on the Water Inrush Coefficient Method. *Mine Water Environ.* **2018**, *37*, 196–204. [CrossRef]
19. Li, B.Y. "Down Three Zones" in the Prediction of the water inrush from Coalbed Floor Aquifer theory, Development and Application. *J. Shandong Inst. Min. Technol.* **1999**, *18*, 11–14.
20. Xue, W.; Wang, S.; Huang, K.; Ji, R.; Liu, M.; Ren, Y.; Xi, X.; Wang, F. Theoretical analysis and field measurement of floor failure in gob side entry of cutting roof in confined water mine area. *J. China Coal Soc.* **2020**, *45*, 581–588. [CrossRef]
21. Tang, C.; Tham, L.; Lee, P.; Yang, T.; Li, L. Coupled analysis of flow, stress and damage (FSD) in rock failure. *Int. J. Rock Mech. Min. Sci.* **2002**, *39*, 477–489. [CrossRef]
22. Lu, H.; Yao, D. Stress distribution and failure depths of layered rock mass of mining floor. *J. Rock Mech. Geotech. Engine* **2014**, *33*, 2030–2039. [CrossRef]
23. Li, A.; Mu, Q.; Ma, L.; Liu, C.; Wang, S.; Wang, F.; Mou, L. Numerical Analysis of the Water-blocking Performance of a Floor with a Composite Structure under Fluid-solid Coupling. *Mine Water Environ.* **2021**, *40*, 479–496. [CrossRef]
24. Li, Z.-H.; Zhang, S.-L.; Du, F. Novel Experimental Model to Investigate Fluid-Solid Coupling in Coal Seam Floor for Water Inrush. *Teh. Vjesn.-Tech. Gaz.* **2018**, *25*, 216–223. [CrossRef]
25. Zhang, B.; Wang, H.; Yuan, L.; Li, S.; Liu, Z. Ultra-low permeability rock-analogue material for gas-solid coupling model tests. *Int. J. Phys. Model. Geotech.* **2021**, *21*, 85–97. [CrossRef]
26. Feng, M.; Mao, X.; Bai, H.; Wang, P.J.C. Experimental research on fracture evolution law of water-resisting strata in coal seam floor above aquifer. *Chin. J. Rock Mech. Eng.* **2009**, *28*, 336–341.
27. Zhang, S.; Guo, W.; Li, Y.; Sun, W.; Yin, D. Experimental Simulation of Fault Water Inrush Channel Evolution in a Coal Mine Floor. *Mine Water Environ.* **2017**, *36*, 443–451. [CrossRef]

28. Cheng, A.P.; Gao, Y.T.; Liu, C.; Chai, J.F. Microseismic Monitoring and Numerical Simulation Research of Floor Failure Depth in Extra-Thick Coal Seam. *Adv. Mater. Res.* **2014**, *881–883*, 1799–1804. [CrossRef]
29. Su, P.; Wei, Z. Depth of Floor Failure of Stope with Medium-Thickness Coal Seam. *Geotech. Geol. Eng.* **2017**, *36*, 1–7. [CrossRef]
30. Gao, Y.; Li, J. Investigation of Rules of Floor Rock Failure in the Workings With Risk of Ordovician Confined Water. *J. China Coal Soc.* **1992**, *17*, 32–39.
31. Gao, Y.; Zhang, Y.; Zhang, H.; Wang, J. Research on Expert System for Risk Assessment of Water Inrush Coal Floor and ITS Application. *Chin. J. Rock Mech. Eng.* **2009**, *28*, 253–258.
32. Wu, Q.; Wang, M.; Wu, X. Investigations of groundwater bursting into coal mine seam floors from fault zones. *Int. J. Rock Mech. Min. Sci.* **2004**, *41*, 557–571. [CrossRef]
33. Wang, Q.; Wang, X.; Hou, Q. Geothermal Water at a Coal Mine: From Risk to Resource. *Mine Water Environ.* **2016**, *35*, 294–301. [CrossRef]
34. Gong, W. Paleo-tectonic Stress Field and Tectonic Evolution since the Mesozoic in the Eastern Mining Area of Pingdingshan. *Earth Sci. Res. J.* **2019**, *23*, 347–357. [CrossRef]
35. Liu, J.; Wang, H.; Jin, D.; Xu, F.; Zhao, C. Hydrochemical characteristics and evolution processes of karst groundwater in Carboniferous Taiyuan formation in the Pingdingshan coalfield. *Environ. Earth Sci.* **2020**, *79*, 151. [CrossRef]
36. Hu, S.; He, L.; Wang, J. Compilation of heat flow data in the continental area of china (3rd edition). *Chin. J. Geophys.* **2001**, *44*, 611–626.
37. Xu, Z.; Elastic Mechanics Brief Tutorial. Elastic Mechanics Brief Tutorial. 2013. Available online: https://xueshu.baidu.com/ndscholar/browse/detail?paperid=e63646c01c0f309fd08f05ba398b36e4&site=xueshu_se (accessed on 12 November 2025).
38. Liang, Z.; Song, W.; Liu, W. Theoretical models for simulating the failure range and stability of inclined floor strata induced by mining and hydraulic pressure. *Int. J. Rock Mech. Min. Sci.* **2020**, *132*, 104382. [CrossRef]
39. Liang, Z.; Song, W. Theoretical and Numerical Investigations of the Failure Characteristics of a Faulted Coal Mine Floor Above a Confined Aquifer. *Mine Water Environ.* **2021**, *40*, 456–465. [CrossRef]
40. Huang, Q.; Wang, X.; Chen, X.; Qin, D.; Chang, Z. Evolution of Interior and Exterior Bearing Structures of the Deep-Soft-Rock Roadway: From Theory to Field Test in the Pingdingshan Mining Area. *Energies* **2020**, *13*, 4357. [CrossRef]
41. Li, A.; Ding, X.; Yu, Z.; Wang, M.; Mu, Q.; Dai, Z.; Li, H.; Zhang, B.; Han, T. Prediction model of fracture depth and water inrush risk zoning in deep mining coal seam floor. *Environ. Earth Sci.* **2022**, *81*, 315. [CrossRef]
42. Song, W.; Liang, Z. Investigation on failure characteristics and water inrush risk of inclined floor mining above confined aquifer. *Rock Soil Mech.* **2020**, *41*, 624–634. [CrossRef]
43. Song, W.; Liang, Z.; Liu, W.; Zhao, C. Theoretical analysis and experimental investigation on failure characteristics and stability of stope floors. *Chin. J. Rock Mech. Eng.* **2019**, *38*, 2208–2218. [CrossRef]
44. Zhao, G.; Xu, W.; Meng, X.; Liu, C. Instability mechanism of high stress rock mass under excavation and unloading induced by disturbance. *J. China Coal Soc.* **2020**, *45*, 936–948. [CrossRef]
45. Zhao, H.; Liu, Y.; Li, J.; Xu, J. Analysis of damage process and zonal failure characteristics of rock mass under floor of isolated coal pillar. *J. China Univ. Min. Technol.* **2021**, *50*, 963–974. [CrossRef]
46. Moussa, A.; Salah, M.A.J. Lemaitre Model to Describe the Behavior of Geotechnical Constructions under Cyclic Loading. *Indian Geotech. J.* **2018**, *48*, 520–528.
47. Cai, Y.; Cao, P.; Mechanics, S. A non-stationary model for rock creep considering damage based on Burgers model. *Rock Soil Mech.* **2016**, *37*, 369–374.
48. Chen, X.; Wang, X.; Zhang, D.; Qin, D.; Wang, Y.; Wang, J.; Chang, Z. Creep and Control of the Deep Soft Rock Roadway (DSRR): Insights from Laboratory Testing and Practice in Pingdingshan Mining Area. *Rock Mech. Rock Eng.* **2022**, *55*, 363–378. [CrossRef]

Disclaimer/Publisher's Note: The statements, opinions and data contained in all publications are solely those of the individual author(s) and contributor(s) and not of MDPI and/or the editor(s). MDPI and/or the editor(s) disclaim responsibility for any injury to people or property resulting from any ideas, methods, instructions or products referred to in the content.